iScience

CellPress
OPEN ACCESS

Article

Flexible Multiplexed In_2O_3 Nanoribbon Aptamer-Field-Effect Transistors for Biosensing

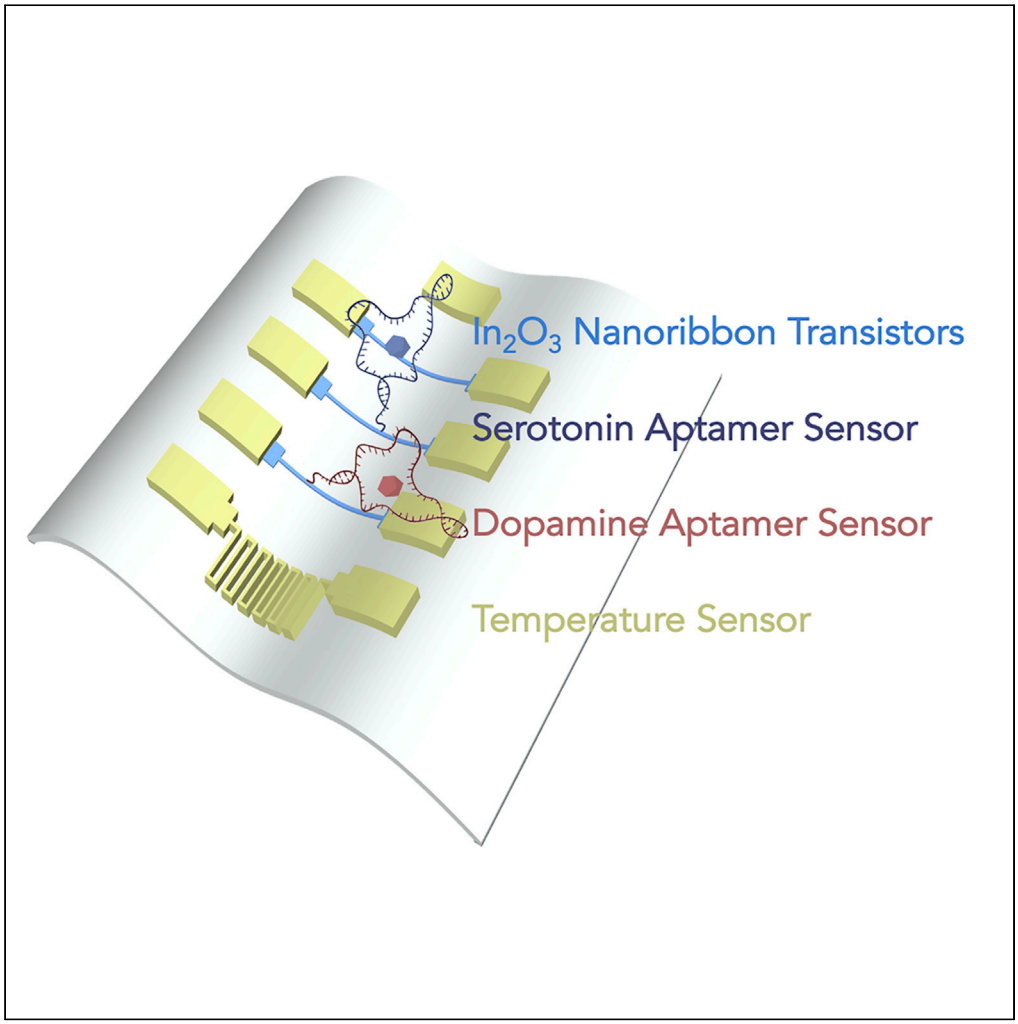

Qingzhou Liu, Chuanzhen Zhao, Mingrui Chen, ..., Paul S. Weiss, Anne M. Andrews, Chongwu Zhou

psw@cnsi.ucla.edu (P.S.W.)
aandrews@mednet.ucla.edu (A.M.A.)
chongwuz@usc.edu (C.Z.)

HIGHLIGHTS

We fabricated flexible In_2O_3 nanoribbon transistors using cleanroom-free processes

Flexible In_2O_3 transistors withstood crumpling and bending with stable performance

Flexible aptamer biosensors detect neurotransmitters in real time

Multiplexed sensors monitor temperature, pH, serotonin, and dopamine simultaneously

Liu et al., iScience *23*, 101469
September 25, 2020 © 2020
https://doi.org/10.1016/j.isci.2020.101469

iScience

CellPress
OPEN ACCESS

Article

Flexible Multiplexed In_2O_3 Nanoribbon Aptamer-Field-Effect Transistors for Biosensing

Qingzhou Liu,[1,2,6] Chuanzhen Zhao,[3,6] Mingrui Chen,[1] Yihang Liu,[2] Zhiyuan Zhao,[1] Fanqi Wu,[1] Zhen Li,[2] Paul S. Weiss,[3,4,*] Anne M. Andrews,[3,5,*] and Chongwu Zhou[1,2,7,*]

SUMMARY

Flexible sensors are essential for advancing implantable and wearable bioelectronics toward monitoring chemical signals within and on the body. Developing biosensors for monitoring multiple neurotransmitters in real time represents a key *in vivo* application that will increase understanding of information encoded in brain neurochemical fluxes. Here, arrays of devices having multiple In_2O_3 nanoribbon field-effect transistors (FETs) were fabricated on 1.4-μm-thick polyethylene terephthalate (PET) substrates using shadow mask patterning techniques. Thin PET-FET devices withstood crumpling and bending such that stable transistor performance with high mobility was maintained over >100 bending cycles. Real-time detection of the small-molecule neurotransmitters serotonin and dopamine was achieved by immobilizing recently identified high-affinity nucleic-acid aptamers on individual In_2O_3 nanoribbon devices. Limits of detection were 10 fM for serotonin and dopamine with detection ranges spanning eight orders of magnitude. Simultaneous sensing of temperature, pH, serotonin, and dopamine enabled integration of physiological and neurochemical data from individual bioelectronic devices.

INTRODUCTION

Electronic devices that extend or create new capabilities for elucidating complex functions in brains (Alivisatos et al., 2013a, 2013b; Weiss, 2013), skin (Gao et al., 2016; Liu et al., 2018b; Kim et al., 2019; Rogers et al., 2019), and other biological systems (Biteen et al., 2016) are of substantial interest. Advances have been made in the areas of soft (Kim et al., 2010; Minev et al., 2015; Wang et al., 2018) and minimally invasive bioelectronics (Rim et al., 2015; Luan et al., 2017; Zhou et al., 2017). Wearable electronics enable sensor systems for monitoring vital signs from skin and biomarkers in sweat, such as ions, glucose, lactase, and cortisol (Kim et al., 2016; Heo et al., 2018; Nyein et al., 2018; Chung et al., 2019; He et al., 2019, 2020; Liu et al., 2020; Torrente-Rodriguez et al., 2020; Yang et al., 2020; Zhao et al., 2020). Efforts have been made toward bioelectronics for implantable devices, including liquid-metal- and hydrogel-based systems (Yu et al., 2016; Fang et al., 2017; Liu et al., 2019; Wen et al., 2019). Soft materials yield readily to pressure and, thus, more closely comply with the pliable and, in some cases, stretchable nature of biological tissues. Fabrication of electronic devices on substrates having low Young's moduli, i.e., greater elasticity, compared with rigid substrates reduces immunological responses after brain implantation (Gunasekera et al., 2015; Kozai et al., 2015). Soft bioelectronics with capabilities to detect multiple neurotransmitters simultaneously and in real time are needed to investigate chemical information processing in brains (Andrews, 2013), particularly in the context of chronic neural recordings (Du et al., 2017).

We have developed aptamer-field-effect transistor (FET) biosensors that detect small molecules, including serotonin, dopamine, glucose, and phenylalanine under high-ionic strength conditions (Nakatsuka et al., 2018b; Cheung et al., 2019). Aptamers are rare, single-stranded nucleic acid sequences isolated from oligonucleotide combinatorial libraries that recognize specific targets (Hamaguchi et al., 2001; Willner et al., 2007; Nakatsuka et al., 2018a). Aptamers can be functionalized to semiconducting materials used in FETs, e.g., organic (Hammock et al., 2013), carbon-based (So et al., 2008; Sorgenfrei et al., 2011), and metal oxides (Kim et al., 2015). Target-induced rearrangement of negatively charged DNA aptamer backbones

[1]Ming Hsieh Department of Electrical Engineering, University of Southern California, Los Angeles, CA 90089, USA

[2]Mork Family Department of Chemical Engineering and Materials Science, University of Southern California, Los Angeles, CA 90089, USA

[3]Department of Chemistry and Biochemistry, California NanoSystems Institute, University of California, Los Angeles, Los Angeles, CA 90095, USA

[4]Departments of Bioengineering and Materials Science and Engineering, University of California, Los Angeles, Los Angeles, CA 90095, USA

[5]Department of Psychiatry and Biobehavioral Sciences, Semel Institute for Neuroscience and Human Behavior, and Hatos Center for Neuropharmacology, University of California, Los Angeles, Los Angeles, CA 90095, USA

[6]Those authors contributed equally

[7]Lead Contact

*Correspondence: psw@cnsi.ucla.edu (P.S.W.), aandrews@mednet.ucla.edu (A.M.A.), chongwuz@usc.edu (C.Z.)

https://doi.org/10.1016/j.isci.2020.101469

results in changes in surface potentials near semiconductor channels to gate FET transconductance (Nakatsuka et al., 2018b). This sensing mechanism is label-free and highly sensitive in physiological environments, e.g., brain tissue, dilute serum.

Metal oxides, such as In_2O_3, have several advantages over other channel materials for FET-based sensors. Similar to Si devices, which can be fabricated with high scalability and uniformity, metal-oxide thin-film transistors have been widely used in industry, e.g., touch screens, displays, solar cells, owing to their electronic performance and large-area uniformity. The main advantages of metal oxides over silicon in wearable sensor applications are the ease of fabrication and compatibility with flexible substrates (Kim, et al., 2015; Rim, et al., 2015; Liu et al., 2018a; Nakatsuka et al., 2018b; Zhao et al., 2018; Cheung, et al., 2019).

Recently, a number of types of flexible electronics, including displays (Lewis et al., 2004; Park et al., 2009), photovoltaics (Fan et al., 2009), and wearable biosensors (Rim, et al., 2015; Liu et al., 2018a), have been fabricated using metal oxides in their structures. The In_2O_3 FETs are well suited to wearable or implantable sensing applications versus a variety of other metal oxides, such as indium-gallium-zinc oxide (IGZO) and ZnO, as the latter are unstable under physiological conditions (Aroonyadet et al., 2015; Jin et al., 2015). For example, ZnO nanoribbon FETs dissolve completely after 14 h of exposure to phosphate buffer saline (PBS). Top-down-fabricated In_2O_3 nanoribbon biosensors, in addition to being stable in physiological solutions, have fast response times, wide detection ranges, low limits of detection, high uniformity, and the capability to be integrated with microfluidics and microprocessors (Aroonyadet, et al., 2015; Liu et al., 2016).

Given the needs for implantable and wearable bioelectronics and the advantageous sensing capabilities of aptamer-FET biosensors under biologically relevant conditions, we aim to advance aptamer-functionalized In_2O_3 FETs in soft, flexible formats. Previously, we fabricated sol-gel processed thin-film In_2O_3 FETs on flexible polyimide for pH and glucose sensing (Rim, et al., 2015). The fabrication process involved spin-coating and high-temperature annealing (>350°C). We have also fabricated In_2O_3 nanoribbon FETs via sputtering at room temperature on thick (~5 μm) polyethylene terephthalate (PET) for wearable applications in enzymatic glucose sensing (Liu et al., 2018a). Here, we advance flexible substrates by fabricating arrays of In_2O_3 nanoribbon FETs on thin (1.4 μm) PET. These new devices exhibited uniform transistor performance, small batch-to-batch variation, and stable performance in high-ionic-strength solutions, i.e., undiluted physiological buffered saline (PBS) and artificial cerebrospinal fluid (aCSF), in a format with robust mechanical flexibility. Thin-film PET-FETs were used to detect serotonin and dopamine over wide concentration ranges, including those occurring in the brain extracellular space (Mathews et al., 2004; Yang et al., 2013, 2015), in real time, and in a multiplexed format that included temperature and pH sensing.

RESULTS

The fabrication process for device arrays on flexible thin-film PET substrates is illustrated in Figure 1A and described in detail in Transparent Methods. Briefly, each 3-inch Si/SiO_2 substrate was spin coated with a 20-μm polydimethylsiloxane (PDMS) adhesion layer. Next, 1.4-μm PET films were adhered to PDMS via van der Waals interactions. Polyethylene terephthalate is a common thermoplastic polymer resin used to make single-use food and liquid containers and polyester clothing fiber. Here, PET films were used as received at room temperature. The current approach has potential for highly scalable and uniform roll-to-roll fabrication.

A shadow mask was used to pattern 16-nm-thick In_2O_3 nanoribbons on PET layers using radio frequency (RF) sputtering. A different shadow mask was then aligned to pattern source, drain, and gate electrodes and temperature sensors each composed of underlying 1-nm Ti layers and overlaying 50-nm Au films. The use of two aligned shadow mask steps eliminated the need for photolithography. The entire fabrication process was completed without the need for a cleanroom. Moreover, this fabrication strategy eliminated photoresist contamination and chemical exposure (Aroonyadet, et al., 2015; Liu, et al., 2016; Liu et al., 2018a). We have used thin metal films on PET for flexible electronics; these films showed high stability and reproducibility (Cao et al., 2016; Liu et al., 2018a). Each patterned PET biosensor film was delaminated from its sacrificial PDMS layer and the FET arrays were used for measurements.

Multiple transistor devices in arrays were fabricated on each 5 cm × 5 cm PET film. Each array consisted of 14 devices (Figure 1B). The total thickness of each array was ~1.5 μm and the total weight was ~2.5 mg.

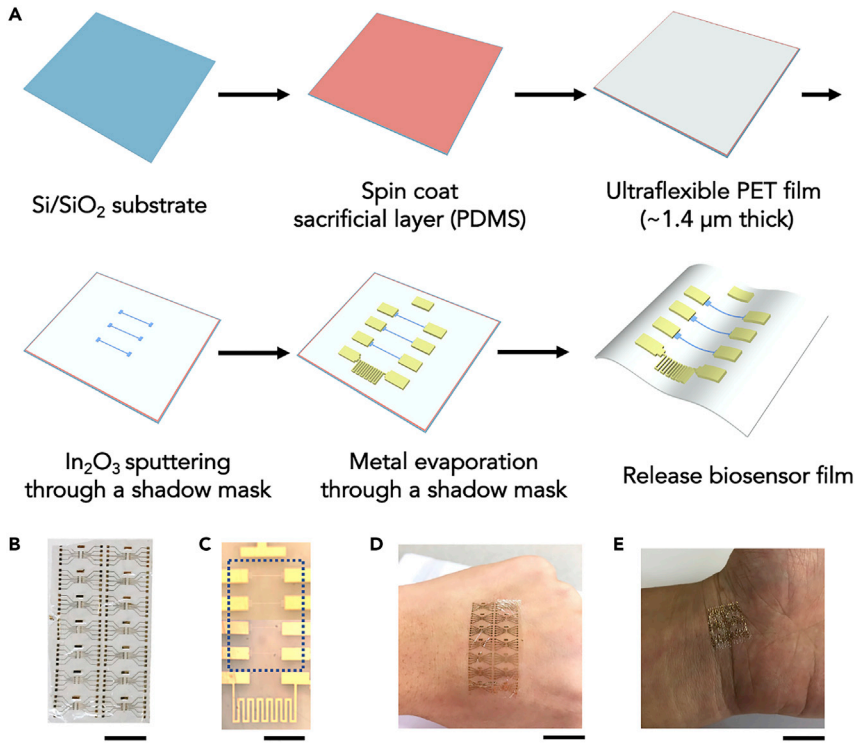

Figure 1. Fabrication of Flexible In_2O_3 Nanoribbon Biosensors

(A) Schematic of the fabrication process. Each Si/SiO_2 substrate was coated with a polydimethylsiloxane (PDMS) adhesion layer. Next, a 1.4-μm polyethylene terephthalate (PET) film was laminated over the PDMS. The In_2O_3 nanoribbons were patterned by sputtering on the PET layer through a shadow mask. A 1-nm Ti adhesion layer followed by a 50-nm Au layer were deposited through a different shadow mask to pattern source, drain, gate, and temperature sensor electrodes. The biosensor film was then delaminated from the rigid carrier wafer.

(B) Photograph of as-fabricated device array. Scale bar is 1 cm. Each array has 14 devices with four field-effect transistors (FETs) per device.

(C) Optical microscope image of a single device showing the Au common-gate electrode, four In_2O_3 nanoribbon FETs (dotted blue box), and a Au resistive temperature sensor (from top to bottom). The low contrast of the In_2O_3 nanoribbons is due to their transparency. Scale bar is 500 μm.

(D) Flexibility of a sensor array is illustrated by conformal attachment to human skin. Scale bar is 2 cm.

(E) Biosensor film wrinkled during human body movement. Scale bar is 1 cm.

See also Figure S1.

Figure 1C shows an individual device containing a Au common gate electrode, four In_2O_3 nanoribbon FETs, and a temperature sensor. Each In_2O_3 nanoribbon was 16 nm thick, 25 μm wide, and 500 μm long (Figure S1). Device arrays were conformally applied to human skin (Figure 1D), illustrating the potential for wearable electronics for healthcare and personal monitoring applications. Devices could be bent and wrinkled when worn on skin (Figure 1E) When used as implantable devices, biosensors may be wrinkled or bent during the insertion process.

The flexible In_2O_3 nanoribbon FET devices exhibited uniform and stable electronic properties under high-ionic-strength conditions. Figure 2A shows the transfer characteristics of a representative In_2O_3 nanoribbon transistor controlled using a common Au gate electrode. Black and blue curves represent drain current-gate voltage (I_{DS}-V_{GS}) characteristics in logarithmic and linear scales, respectively, and indicate gate modulation of drain current in phosphate buffered saline (PBS) with a current on/off ratio of $\sim 10^3$. The corresponding output characteristics demonstrated that the devices exhibited FET behavior typically associated with drain voltage modulation (Figure 2B). The gate leakage current was negligible compared with the drain-source current. As an example, the gate leakage current was less than 2 nA at V_{DS} = 0.2 V (Figure S2). All transistors in a representative array were characterized. Nearly 100% were functional (55/56) with only one transistor showing significantly lower mobility compared with the other transistors.

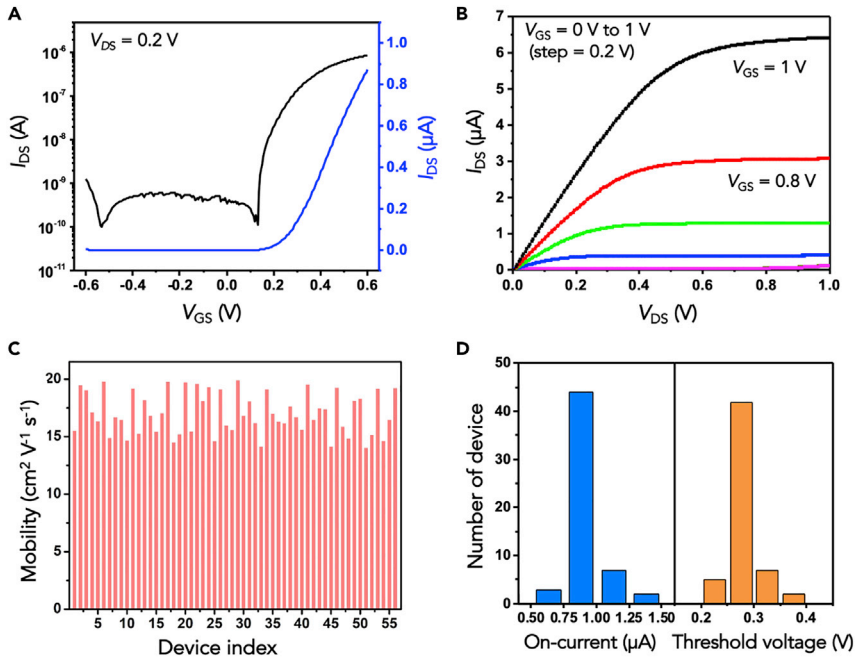

Figure 2. Electronic Performance of Flexible In_2O_3 Nanoribbon Field-Effect Transistors

(A) Representative transfer characteristics of an In_2O_3 nanoribbon transistor with L = 500 μm, W = 25 μm, and H = 16 μm in phosphate buffered saline. The I_D (drain current) is shown in a logarithmic scale (left, black trace) and a linear scale (right, blue trace); V_{GS} is the gate-source voltage. The applied drain-source voltage V_{DS} was 0.2 V.

(B) Output curves in the linear and saturation regimes. In this plot, I_{DS} is a function of V_{DS} with V_{GS} from 0 to 1 V in 0.2-V steps.

(C) Plot of the charge-carrier mobilities of 56 transistors in an array.

(D) Histograms showing on-currents and threshold voltages from the same 56 transistors. The average mobility was 17.8 ± 1.8 $cm^2 V^{-1} s^{-1}$. The average on-current was 0.86 ± 0.1 μA. The average threshold voltage was 0.27 ± 0.02 V. See also Figure S2.

The charge-carrier mobilities of 56 transistors in a single array were measured and calculated (details in Transparent Methods) and showed ~10% variability (Figure 2C), with an average mobility of 17.8 ± 1.8 $cm^2 V^{-1} s^{-1}$. Figure 2D shows a histogram of the on-state currents and threshold voltages of the 56 devices. Both showed narrow distributions. Notably, In_2O_3 nanoribbon transistors exhibited uniform and stable electronic performance in a physiological environment (all data in Figure 2 were collected in undiluted PBS) at relatively low voltages (<1 V). These characteristics are favorable for implantable neural recording devices and on-skin electronics.

Mechanical flexibility of In_2O_3 nanoribbon FETs was evaluated in experiments that involved bending and crumpling. Figure 3A shows a photograph of a PET sheet patterned with In_2O_3 FETs tightly wrapped around a copper wire having a radius of 100 μm. Under these conditions, a tensile strain of ~0.75% (calculations in Transparent Methods) was applied to the In_2O_3 nanoribbons with the direction of strain parallel to the current flow. In another test, a 5 cm × 5 cm PET sheet of In_2O_3 FET devices was tightly crumpled for ~5 s (Figure 3B), then flattened for electronic measurements.

The electronic performance of In_2O_3 FETs while bent and after crumpling was measured in PBS. Typical transfer curves of representative devices in the relaxed state, bent with a radius curvature of ~0.1 mm, and after 100 crumpling cycles are shown in Figure 3C. Figures 3D and 3E show mobilities and threshold voltages averaged over 15 devices after 5, 10, 50, and 100 bending or crumpling cycles, respectively. After 100 bending cycles, the change in average mobility was 5.6% (from 18.4 to 17.3 $cm^2 V^{-1} s^{-1}$); the threshold voltage showed only a small variation from 0.23 to 0.27 V. Similar results were observed in repeated crumpling tests. The change in mobility was 6.1% after 100 crumpling cycles, and the threshold voltage remained around 0.26 V. Together, these findings illustrate that the In_2O_3 nanoribbon FET devices fabricated on thin-film PET are suitable for flexible electronics with reliable performance even under

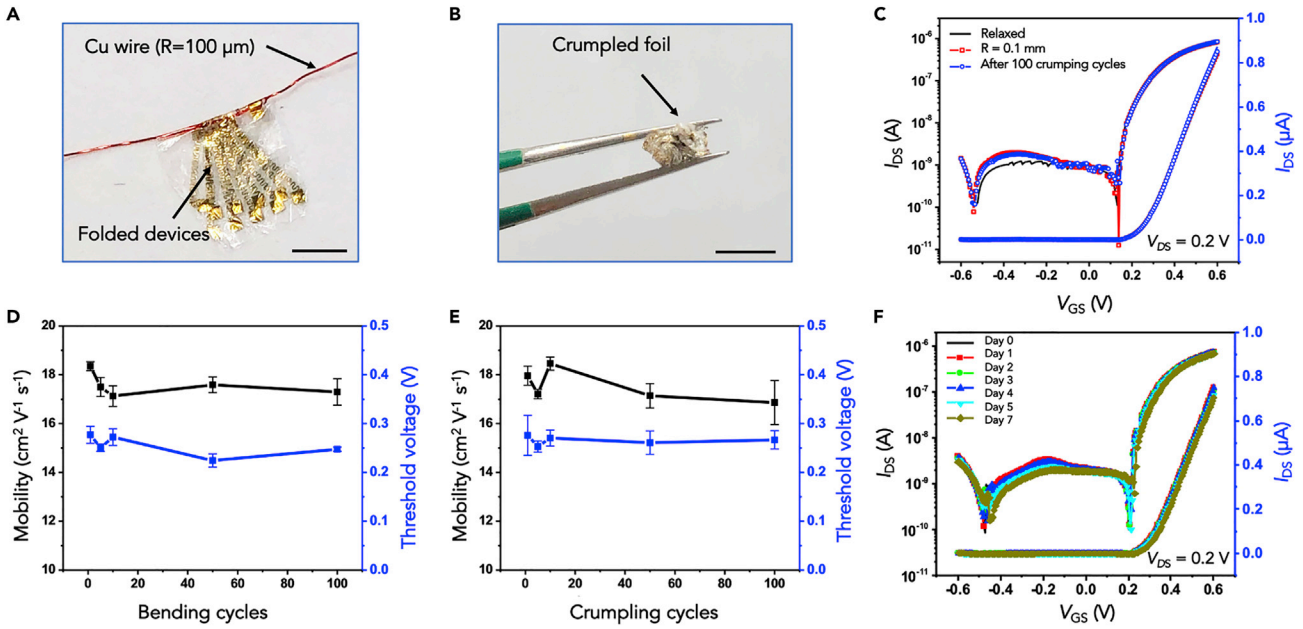

Figure 3. Stability of Flexible In_2O_3 Nanoribbon Sensors

(A) Photograph of flexible thin-film (1.4-μm) PET In_2O_3 sensor arrays wrapped around a copper wire with a radius of 100 μm. Scale bar is 5 mm.

(B) Photograph of a crumpled In_2O_3 biosensor film (original size: 5 cm × 5 cm). Scale bar is 0.5 cm.

(C–E) (C) Transfer characteristics of a representative In_2O_3 transistor in a relaxed state, bent around a copper wire with a radius of ~0.1 mm, and after crumpling, respectively. Mobilities (left) and threshold voltages (right) obtained in a relaxed state (D) after different numbers of bending cycles and (E) after various numbers of crumpling cycles.

(F) Transfer characteristics of an In_2O_3 transistor measured immediately after fabrication (Day 0) and after immersion in undiluted PBS for 1, 2, 3, 4, 5, and 7 day(s). Error bars in (D) and (E) are standard deviations of N = 15 devices.

extreme bending and crumpling cycles. Bending events are common for both wearable bioelectronics and implantable devices. For example, bending occurs in and on soft tissue where devices need to adapt to movement.

Figure 3F shows transfer curves for FET devices before and after immersion in PBS for 1, 2, 3, 4, 5, or 7 day(s). Based on data in logarithmic and linear scales, there were no significant changes in FET performance. These findings substantiate the long-term stability of In_2O_3 transistors in high-ionic-strength solutions and indicate that these sensors are robust for at least 1 week when exposed to physiological fluids.

A portion of the negatively charged backbone of the serotonin aptamer used herein is hypothesized to move away from In_2O_3 channel surfaces upon target capture (Figure 4A) (Nakatsuka et al., 2018b). Thus, the electrostatic repulsion between the electrons in an *n*-type semiconductor channel and negatively charged aptamers decreases and channel conductance increases in response to aptamer-target association. Results for serotonin detection using In_2O_3 nanoribbon FETs functionalized with serotonin aptamers are shown in Figure 4B. Details of the surface functionalization and aptamer sequences are in Transparent Methods.

To evaluate sensor reliability in a high-ionic-strength buffer that approximates the brain extracellular fluid, serotonin was dissolved in artificial cerebrospinal fluid (aCSF). Devices were operated at a 0.25-V gate bias applied using the Au common gate electrode. Entire devices, including the channels, were submerged in aCSF to obtain baseline currents. After changing the solution to 10 fM serotonin in aCSF, the sensing signal increased by ~1% after stabilization (~150 s). As the solutions over the FETs were changed to include higher serotonin concentrations ranging from 0.1 pM to 1 μM sequentially, stepwise I_{DS} increases were observed (Figure 4B).

To test reproducibility of detection, we conducted sensing with nine different devices. The relationship between serotonin concentration and saturated current response is shown in Figure 4C. We performed the

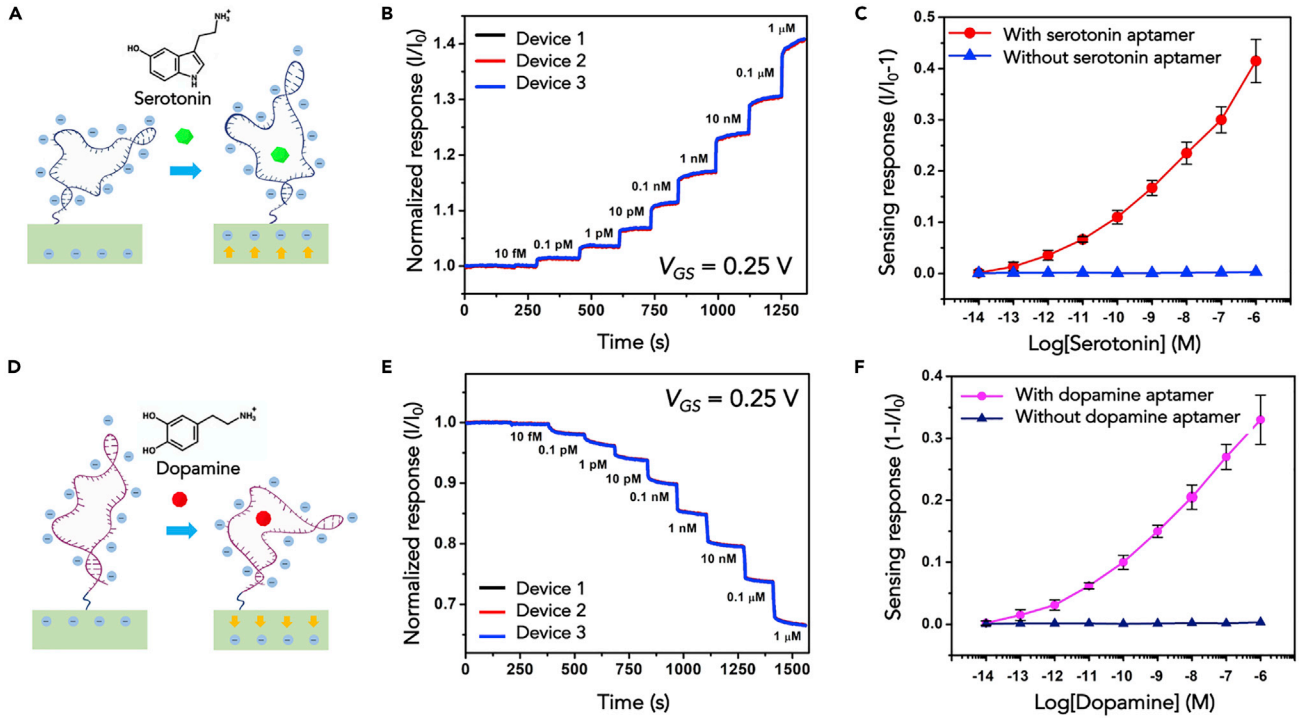

Figure 4. Characterization of Serotonin- and Dopamine-Aptamer-Functionalized Sensors

(A) Some aptamers, such as the aptamer used here to recognize serotonin, reorient a portion of their backbones away from semiconductor channels upon target binding, thereby increasing transconductance for *n*-type semiconductors.

(B) Normalized (I/I_0; unitless) real-time sensing results from three In_2O_3 nanoribbon biosensors functionalized with the serotonin aptamer. Devices showed responses to serotonin (in undiluted artificial cerebrospinal fluid) at concentrations ranging from 10 fM to 1 μM.

(C) Relationship between serotonin concentration and current responses from nine different devices. Results from unfunctionalized devices lacking aptamers are plotted for comparison.

(D) Other aptamers, such as the dopamine aptamer used here, reorient a portion of their negatively charged oligonucleotide backbones closer to field-effect transistors upon target recognition to deplete channels electrostatically.

(E) Normalized (I/I_0; unitless) real-time sensing results from three In_2O_3 nanoribbon biosensors functionalized with the dopamine aptamer. Devices showed responses to dopamine (in undiluted artificial cerebrospinal fluid) at concentrations ranging from 10 fM to 1 μM.

(F) Relationship between dopamine concentration and current responses from nine different devices. Results from devices lacking the dopamine aptamer are also plotted. All devices were operated with V_{DS} = 0.2 V and V_{GS} = 0.25 V. Errors bars in (C) and (F) are standard deviations for N = 9 devices (from three separate substrates where each substrate had three devices) and are too small to be visualized in some cases.

See also Figures S3–S5.

same sensing procedure on control devices, i.e., those with surface functionalization *sans* aptamers (Figure S3). The latter results are plotted in Figure 4C for comparison and showed minimal signal compared with that of FETs functionalized with aptamers. A device functionalized with a scrambled serotonin aptamer sequence also showed minimal response to serotonin indicating target selectivity (Figure S4).

In contrast to the serotonin aptamer, a portion of the negatively charged backbone of the dopamine aptamer used here is hypothesized to move closer to *n*-type semiconductor channels upon dopamine binding, thus increasing electrostatic repulsion and decreasing the In_2O_3 transconductance (Figure 4D) (Nakatsuka et al., 2018b). The results of real-time dopamine sensing are shown in Figure 4E, and a summary of the relationship between dopamine concentrations and the corresponding FET responses from nine different devices is plotted in Figure 4F. The limit of detection for dopamine sensing was also on the order of 10 fM. Data were collected every 2 s and indicated that aptamer-FETs have ~5-s response times (Figure S5). Our determination of response time was limited by the semiconductor analyzer and software, thus measured response times are an upper limit.

We fabricated flexible sensing devices with the capability to monitor temperature, pH, serotonin, and dopamine simultaneously in real time. We performed sensing while devices were conformally applied to

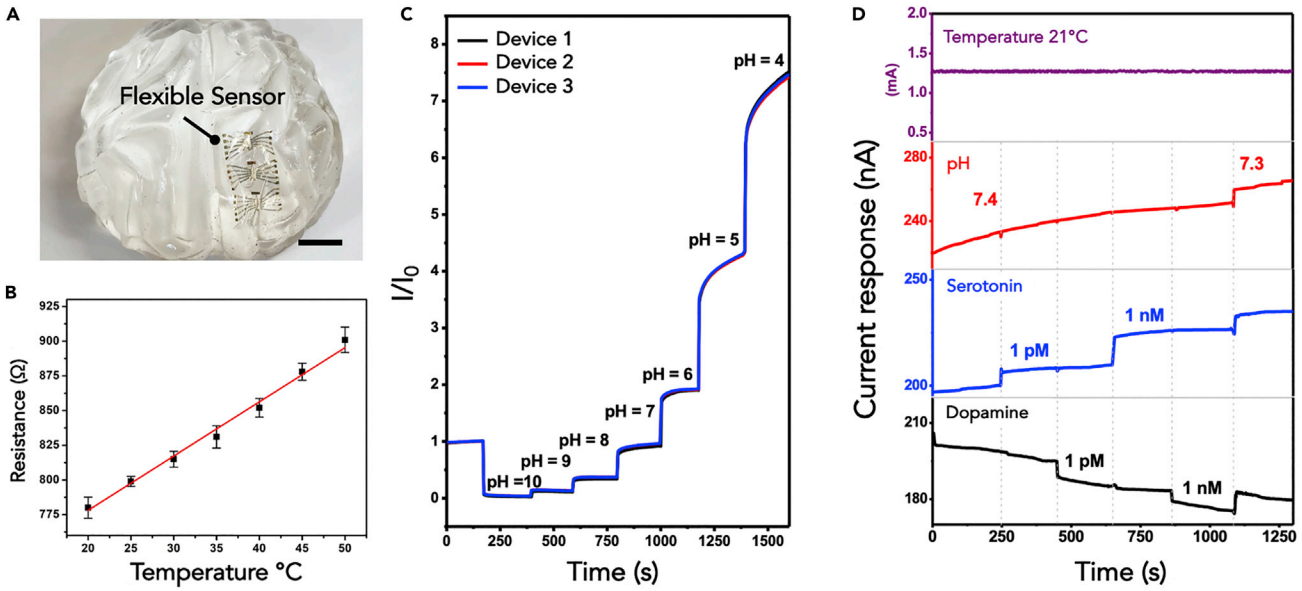

Figure 5. Multiplexed Biosensing

(A) Photograph of three sensor devices attached conformally to a polydimethylsiloxane brain mimic. Scale bar is 1 cm.

(B) Changes in resistance with respect to temperature in artificial cerebrospinal fluid (aCSF). Error bars are standard deviations for $N = 5$ devices. For linear regression (y = ax + b), resistance = (3.9×temperature) + 700, where temperature is in degrees Celsius; $R^2 = 0.99$.

(C) Real-time pH sensing at unfunctionalized In_2O_3 nanoribbons in three different devices exposed to buffer solutions with pH values from 10 to 4.

(D) Simultaneous sensing of temperature, pH, serotonin, and dopamine in aCSF (pH = 7.4). Two adjacent devices were simultaneously exposed to solutions of 1 pM serotonin, 1 pM dopamine, 1 nM serotonin, and 1 nM dopamine, sequentially. Only transistors functionalized with the respective target-specific aptamers responded to the corresponding targets. All sensors responded to a pH change in aCSF (7.4–7.3). The devices were operated at $V_{DS} = 0.2$ V and $V_{GS} = 0.25$ V.

the surface of an "artificial brain," a brain replica made from PDMS, as a demonstration of working on/in irregular tissue surfaces (Figure 5A). The sensors developed here could be used as implanted or surface brain sensors or as wearable biosensors on the skin.

Local temperature change monitoring provides useful intraparenchymal and superficial information. For example, internal brain temperature is an indicator of neural functional activity (Wang et al., 2014). Brain temperature is regionally specific and fluctuates by as much at 4 °C under normal activation states. Clinical studies indicate a relationship between brain temperature changes and cerebral injury (Nielsen et al., 2013). Moreover, therapeutics, e.g., anesthesia, drugs of abuse, cause large and sometimes devastating changes in brain temperature, in the case of the latter (Kiyatkin, 2018). Skin temperature is also considered clinically informative, where it has been linked to a variety of diseases and skin injuries (Sprigle et al., 2001; Webb et al., 2013). Therefore, sensing devices with integrated temperature sensors provide information to supplement target molecule monitoring.

Thermistors fabricated from Au wires have been used as temperature indicators in wearable sensor systems (Gao, et al., 2016). Here, we adapted a similar design and integrated fabrication within the shadow mask designs. Figure 5B shows the resistance of a representative Au thermistor in PBS ranging from 20°C to 50°C with 5°C increments. The measured resistances were highly correlated with changes in temperature at a sensitivity of ~4 Ω/°C.

Field-effect transistor sensors are sensitive to pH changes, i.e., $[H^+]$, because sensing mechanisms involve detecting changes in charge close to semiconductor surfaces (Aroonyadet, et al., 2015; Rim, et al., 2015; Liu, et al., 2016). Fluctuations in brain pH occur as a result of changes in CO_2 levels, i.e., carbonic acid, which increase in conjunction with neural activity, neurotransmitter release, and oxygen consumption (Meunier et al., 2018). Sensing pH is useful in wearable bioelectronics as sweat pH values also vary owing to changes in carbonic acid levels (Gao, et al., 2016). Monitoring pH in sweat can be indicative of variations in electrolyte concentrations, which are biomarkers of disease and metabolic activity (Patterson

et al., 2000; Burry et al., 2001; Sonner et al., 2015; Lee et al., 2017). Here, unfunctionalized In_2O_3 nanoribbons responded to pH in buffer solutions ranging from pH 10 to pH 4 (Figure 5C). Devices showed increases in conductance when the pH of solutions decreased, corresponding to a positive gating effect at *n*-type In_2O_3 transistors (Aroonyadet, et al., 2015; Rim, et al., 2015; Liu, et al., 2016). We note that, in addition to unfunctionalized FETs, devices functionalized with aptamers can be pH sensitive (Idili et al., 2014; Porchetta et al., 2015; Gordon et al., 2018). As pH decreases, negatively charged oligonucleotide backbones become associated with larger numbers of protons changing local charge near semiconductor surfaces.

Including pH sensors in our devices enabled discriminating target-specific changes in transconductance at aptamer-functionalized sensors from those associated with local pH changes. Three devices from adjacent groups on the same substrate array were used for multiplexed sensing. One device was functionalized with the serotonin aptamer to work as a serotonin sensor. Another device next to the serotonin sensor was protected by a PDMS mask during the aptamer functionalization. After that, the PDMS mask was removed, and this device consisting of unfunctionalized FETs was used as a pH sensor. A third device from an adjacent group of devices was functionalized with the dopamine aptamer and was used as a dopamine sensor. Lastly, a patterned gold wire thermistor on the same substrate was used as a temperature sensor.

After obtaining a stable baseline current in aCSF (pH 7.4), solutions above FETs were sequentially replaced with aCSF containing 1 pM serotonin, 1 pM dopamine, 1 nM serotonin, or 1 nM dopamine. The two aptamer-functionalized devices detected and differentiated physiologically relevant concentrations of serotonin and dopamine, simultaneously (Figure 5D). No current changes occurred at the pH-sensing FETs in response to the addition of serotonin or dopamine. In contrast, when aCSF (pH 7.3) *sans* neurotransmitters was introduced at t = 1,100 s, all three devices showed responses to a 0.1 pH unit change. For physiological sensing applications where pH and neurotransmitter concentrations change simultaneously, neurotransmitter-specific FET responses can be distinguished by subtracting responses occurring at pH sensors.

The directions of change for the I_{DS}-*t* curves (Figures 4B, 4E, and 5D) are consistent with our hypotheses regarding the different types of conformational changes for these particular serotonin and dopamine aptamers and provide complementary and straightforward evidence of aptamer sensing mechanisms (Nakatsuka et al., 2018b). These serotonin and dopamine aptamers have been previously characterized for selectivity in fluorescence and FET sensing formats (Nakatsuka et al., 2018b). Both aptamers showed high selectivity for their targets versus structurally similar precursors and metabolites found at high concentrations in the brain extracellular space. We also previously investigated serotonin-aptamer FET sensor stability in brain tissue (Nakatsuka et al., 2018b). Although baseline sensor responses changed after tissue exposure, calibrated responses, which correct for baseline drift, were stable and sensitive over a large range of serotonin concentrations even after 12 h of brain tissue exposure. Moreover, we have used glucose- and phenylalanine-aptamer FETs to sense their respective targets at physiological concentrations in serum diluted with Ringer's buffer, which mimics the ionic composition of plasma (Nakatsuka et al., 2018b; Cheung, et al., 2019).

DISCUSSION

We have demonstrated flexible conformal sensor devices for multiplexed and selective detection of neurotransmitters and other key physiological parameters. Devices displayed excellent flexibility when mechanically deformed and long-term stability in high-ionic-strength solutions. Real-time sensing of neurotransmitters at low, physiologically relevant concentrations was demonstrated. These sensors can be combined with integrated circuits for device operation and signal processing for wearable or implantable applications. To overcome spatial limitations for functionalization with different aptamers, an electrochemical approach to addressing different FETs in the same device can be applied for future studies (Curreli et al., 2005). In sum, the current findings illustrate multiplexed, temporally resolved FET sensing of targets over large physiologically relevant concentration ranges, under high-ionic-strength conditions, and in a robust, flexible format. In conjunction with previous demonstrations of selectivity and sensing in biological tissues, small-molecule physiological sensors are expected to advance our understanding of the brain and other biological systems.

Limitations of the Study

Experiments to investigate interference by ascorbic acid and uric acid were not included in this work and require further investigation.

Resource Availability

Lead Contact

Further information and requests for resources and reagents should be directed to and will be fulfilled by the Lead Contact, Professor Chongwu Zhou (chongwuz@usc.edu)

Materials Availability

This study did not generate new unique reagents.

Data and Code Availability

This study did not generate/analyze datasets/code.

METHODS

All methods can be found in the accompanying Transparent Methods supplemental file.

SUPPLEMENTAL INFORMATION

Supplemental Information can be found online at https://doi.org/10.1016/j.isci.2020.101469.

ACKNOWLEDGMENTS

C.Zhao, A.M.A., and P.S.W. acknowledge support from the National Institute on Drug Abuse (DA045550). C.Zhou acknowledges support from King Abdulaziz City for Science and Technology (KACST) via The Center of Excellence for Nanotechnologies (CEGN). The authors thank Dr. Kevin M. Cheung for helpful feedback on the manuscript.

AUTHOR CONTRIBUTIONS

Data were collected by Q.L., C. Zhao, M.C., Y.L., Z.Z., F.W., and Z.L. and analyzed by Q.L., C. Zhao, A.M.A., and C. Zhou. Figures were prepared by Q.L. and C. Zhao. The manuscript was written by Q.L., C. Zhao, P.S.W., A.M.A., and C. Zhou with assistance from all authors. All authors have read, corrected, and approved the final version of the manuscript.

DECLARATION OF INTERESTS

Stem-loop receptor-based field effector sensor devices for sensing at physiological salt concentration. Co-inventors: A. M. Andrews, P. S. Weiss, N. Nakatsuka, M. N. Stojanović, and K. A. Yang, nonprovisional U.S. and foreign patents filed 2019. PCT/US2019/046891.

Received: June 24, 2020
Revised: August 3, 2020
Accepted: August 13, 2020
Published: September 25, 2020

REFERENCES

Alivisatos, A.P., Andrews, A.M., Boyden, E.S., Chun, M., Church, G.M., Deisseroth, K., Donoghue, J.P., Fraser, S.E., Lippincott-Schwartz, J., Looger, L.L., et al. (2013a). Nanotools for neuroscience and brain activity mapping. ACS Nano *7*, 1850–1866.

Alivisatos, A.P., Chun, M., Church, G.M., Deisseroth, K., Donoghue, J.P., Greenspan, R.J., McEuen, P.L., Roukes, M.L., Sejnowski, T.J., Weiss, P.S., et al. (2013b). The brain activity map. Science *339*, 1284–1285.

Andrews, A.M. (2013). The brain initiative: toward a chemical connectome. ACS Chem. Neurosci. *4*, 645.

Aroonyadet, N., Wang, X., Song, Y., Chen, H., Cote, R.J., Thompson, M.E., Datar, R.H., and Zhou, C. (2015). Highly scalable, uniform, and sensitive biosensors based on top-down indium oxide nanoribbons and electronic enzyme-linked immunosorbent assay. Nano Lett. *15*, 1943–1951.

Biteen, J.S., Blainey, P.C., Cardon, Z.G., Chun, M., Church, G.M., Dorrestein, P.C., Fraser, S.E., Gilbert, J.A., Jansson, J.K., Knight, R., et al. (2016). Tools for the microbiome: nano and beyond. ACS Nano *10*, 6–37.

Burry, J.S., Coulson, H.F., Esser, I., Marti, V., Melling, S.J., Rawlings, A.V., Roberts, G., and Mills, A.K. (2001). Erroneous gender differences in axillary skin surface/sweat pH. Int. J. Cosmet. Sci. *23*, 99–107.

Cao, X., Cao, Y., and Zhou, C. (2016). Imperceptible and ultraflexible *p*-type transistors

and macroelectronics based on carbon nanotubes. ACS Nano *10*, 199–206.

Cheung, K.M., Yang, K.A., Nakatsuka, N., Zhao, C., Ye, M., Jung, M.E., Yang, H., Weiss, P.S., Stojanovic, M.N., and Andrews, A.M. (2019). Phenylalanine monitoring *via* aptamer-field-effect transistor sensors. ACS Sens. *4*, 3308–3317.

Chung, H.U., Kim, B.H., Lee, J.Y., Lee, J., Xie, Z., Ibler, E.M., Lee, K., Banks, A., Jeong, J.Y., Kim, J., et al. (2019). Binodal, wireless epidermal electronic systems with in-sensor analytics for neonatal intensive care. Science *363*, eaau0780.

Curreli, M., Li, C., Sun, Y., Lei, B., Gundersen, M.A., Thompson, M.E., and Zhou, C. (2005). Selective functionalization of In_2O_3 nanowire mat devices for biosensing applications. J. Am. Chem. Soc. *127*, 6922–6923.

Du, Z.J., Kolarcik, C.L., Kozai, T.D.Y., Luebben, S.D., Sapp, S.A., Zheng, X.S., Nabity, J.A., and Cui, X.T. (2017). Ultrasoft microwire neural electrodes improve chronic tissue integration. Acta Biomater. *53*, 46–58.

Fan, Z., Razavi, H., Do, J.W., Moriwaki, A., Ergen, O., Chueh, Y.L., Leu, P.W., Ho, J.C., Takahashi, T., Reichertz, L.A., et al. (2009). Three-dimensional nanopillar-array photovoltaics on low-cost and flexible substrates. Nat. Mater. *8*, 648–653.

Fang, H., Yu, K.J., Gloschat, C., Yang, Z., Chiang, C.H., Zhao, J., Won, S.M., Xu, S., Trumpis, M., Zhong, Y., et al. (2017). Capacitively coupled arrays of multiplexed flexible silicon transistors for long-term cardiac electrophysiology. Nat. Biomed. Eng. *1*, 0038.

Gao, W., Emaminejad, S., Nyein, H.Y.Y., Challa, S., Chen, K., Peck, A., Fahad, H.M., Ota, H., Shiraki, H., Kiriya, D., et al. (2016). Fully integrated wearable sensor arrays for multiplexed *in situ* perspiration analysis. Nature *529*, 509–514.

Gordon, C.K.L., Eisenstein, M., and Soh, H.T. (2018). Direct selection strategy for isolating aptamers with pH-sensitive binding activity. ACS Sens. *3*, 2574–2580.

Gunasekera, B., Saxena, T., Bellamkonda, R., and Karumbaiah, L. (2015). Intracortical recording interfaces: current challenges to chronic recording function. ACS Chem. Neurosci. *6*, 68–83.

Hamaguchi, N., Ellington, A., and Stanton, M. (2001). Aptamer beacons for the direct detection of proteins. Anal. Biochem. *294*, 126–131.

Hammock, M.L., Knopfmacher, O., Naab, B.D., Tok, J.B.H., and Bao, Z.A. (2013). Investigation of protein detection parameters using nanofunctionalized organic field-effect transistors. ACS Nano *7*, 3970–3980.

He, X., Xu, T., Gu, Z., Gao, W., Xu, L.P., Pan, T., and Zhang, X. (2019). Flexible and superwettable bands as a platform toward sweat sampling and sensing. Anal. Chem. *91*, 4296–4300.

He, X., Yang, S., Pei, Q., Song, Y., Liu, C., Xu, T., and Zhang, X. (2020). Integrated smart janus textile bands for self-pumping sweat sampling and analysis. ACS Sens. *5*, 1548–1554.

Heo, S.Y., Kim, J., Gutruf, P., Banks, A., Wei, P., Pielak, R., Balooch, G., Shi, Y., Araki, H., Rollo, D., et al. (2018). Wireless, battery-free, flexible, miniaturized dosimeters monitor exposure to solar radiation and to light for phototherapy. Sci. Transl. Med. *10*, eaau1643.

Idili, A., Vallee-Belisle, A., and Ricci, F. (2014). Programmable pH-triggered DNA nanoswitches. J. Am. Chem. Soc. *136*, 5836–5839.

Jin, S.H., Kang, S.K., Cho, I.T., Han, S.Y., Chung, H.U., Lee, D.J., Shin, J., Baek, G.W., Kim, T.I., Lee, J.H., et al. (2015). Water-soluble thin film transistors and circuits based on amorphous indium-gallium-zinc oxide. ACS Appl. Mater. Interfaces *7*, 8268–8274.

Kim, D.H., Viventi, J., Amsden, J.J., Xiao, J., Vigeland, L., Kim, Y.S., Blanco, J.A., Panilaitis, B., Frechette, E.S., Contreras, D., et al. (2010). Dissolvable films of silk fibroin for ultrathin conformal bio-integrated electronics. Nat. Mater. *9*, 511–517.

Kim, J., Rim, Y.S., Chen, H.J., Cao, H.H., Nakatsuka, N., Hinton, H.L., Zhao, C.Z., Andrews, A.M., Yang, Y., and Weiss, P.S. (2015). Fabrication of high-performance ultrathin In_2O_3 film field-effect transistors and biosensors using chemical lift-off lithography. ACS Nano *9*, 4572–4582.

Kim, J., Jeerapan, I., Imani, S., Cho, T.N., Bandodkar, A., Cinti, S., Mercier, P.P., and Wang, J. (2016). Noninvasive alcohol monitoring using a wearable tattoo-based iontophoretic-biosensing system. ACS Sens. *1*, 1011–1019.

Kim, J., Campbell, A.S., de Avila, B.E., and Wang, J. (2019). Wearable biosensors for healthcare monitoring. Nat. Biotechnol. *37*, 389–406.

Kiyatkin, E.A. (2018). Brain temperature: from physiology and pharmacology to neuropathology. Handb. Clin. Neurol. *157*, 483–504.

Kozai, T.D., Jaquins-Gerstl, A.S., Vazquez, A.L., Michael, A.C., and Cui, X.T. (2015). Brain tissue responses to neural implants impact signal sensitivity and intervention strategies. ACS Chem. Neurosci. *6*, 48–67.

Lee, H., Song, C., Hong, Y.S., Kim, M.S., Cho, H.R., Kang, T., Shin, K., Choi, S.H., Hyeon, T., and Kim, D.H. (2017). Wearable/disposable sweat-based glucose monitoring device with multistage transdermal drug delivery module. Sci. Adv. *3*, e1601314.

Lewis, J., Grego, S., Chalamala, B., Vick, E., and Temple, D. (2004). Highly flexible transparent electrodes for organic light-emitting diode-based displays. Appl. Phys. Lett. *85*, 3450–3452.

Liu, C., Xu, T., Wang, D., and Zhang, X. (2020). The role of sampling in wearable sweat sensors. Talanta *212*, 120801.

Liu, Q., Aroonyadet, N., Song, Y., Wang, X., Cao, X., Liu, Y., Cong, S., Wu, F., Thompson, M.E., and Zhou, C. (2016). Highly sensitive and quick detection of acute myocardial infarction biomarkers using In_2O_3 nanoribbon biosensors fabricated using shadow masks. ACS Nano *10*, 10117–10125.

Liu, Q., Liu, Y., Wu, F., Cao, X., Li, Z., Alharbi, M., Abbas, A.N., Amer, M.R., and Zhou, C. (2018a). Highly sensitive and wearable In_2O_3 nanoribbon transistor biosensors with integrated on-chip gate for glucose monitoring in body fluids. ACS Nano *12*, 1170–1178.

Liu, Z., Qi, D., Leow, W.R., Yu, J., Xiloyannnis, M., Cappello, L., Liu, Y., Zhu, B., Jiang, Y., Chen, G., et al. (2018b). 3D-structured stretchable strain sensors for out-of-plane force detection. Adv. Mater. *30*, e1707285.

Liu, Y., Liu, J., Chen, S., Lei, T., Kim, Y., Niu, S., Wang, H., Wang, X., Foudeh, A.M., Tok, J.B., et al. (2019). Soft and elastic hydrogel-based microelectronics for localized low-voltage neuromodulation. Nat. Biomed. Eng. *3*, 58–68.

Luan, L., Wei, X.L., Zhao, Z.T., Siegel, J.J., Potnis, O., Tuppen, C.A., Lin, S.Q., Kazmi, S., Fowler, R.A., Holloway, S., et al. (2017). Ultraflexible nanoelectronic probes form reliable, glial scar-free neural integration. Sci. Adv. *3*, e1601966.

Mathews, T.A., Fedele, D.E., Coppelli, F.M., Avila, A.M., Murphy, D.L., and Andrews, A.M. (2004). Gene dose-dependent alterations in extraneuronal serotonin but not dopamine in mice with reduced serotonin transporter expression. J. Neurosci. Methods *140*, 169–181.

Meunier, C.J., Mitchell, E.C., Roberts, J.G., Toups, J.V., McCarty, G.S., and Sombers, L.A. (2018). Electrochemical selectivity achieved using a double voltammetric waveform and partial least squares regression: differentiating endogenous hydrogen peroxide fluctuations from shifts in pH. Anal. Chem. *90*, 1767–1776.

Minev, I.R., Musienko, P., Hirsch, A., Barraud, Q., Wenger, N., Moraud, E.M., Gandar, J., Capogrosso, M., Milekovic, T., Asboth, L., et al. (2015). Electronic dura mater for long-term multimodal neural interfaces. Science *347*, 159–163.

Nakatsuka, N., Cao, H.H., Deshayes, S., Melkonian, A.L., Kasko, A.M., Weiss, P.S., and Andrews, A.M. (2018a). Aptamer recognition of multiplexed small-molecule-functionalized substrates. ACS Appl. Mater. Interfaces *10*, 23490–23500.

Nakatsuka, N., Yang, K.A., Abendroth, J.M., Cheung, K.M., Xu, X., Yang, H., Zhao, C., Zhu, B., Rim, Y.S., Yang, Y., et al. (2018b). Aptamer-field-effect transistors overcome Debye length limitations for small-molecule sensing. Science *362*, 319–324.

Nielsen, N., Wetterslev, J., Cronberg, T., Erlinge, D., Gasche, Y., Hassager, C., Horn, J., Hovdenes, J., Kjaergaard, J., Kuiper, M., et al. (2013). Targeted temperature management at 33°C versus 36°C after cardiac arrest. N. Engl. J. Med. *369*, 2197–2206.

Nyein, H.Y.Y., Tai, L.C., Ngo, Q.P., Chao, M., Zhang, G.B., Gao, W., Bariya, M., Bullock, J., Kim, H., Fahad, H.M., et al. (2018). A wearable microfluidic sensing patch for dynamic sweat secretion analysis. ACS Sens. *3*, 944–952.

Park, J.S., Kim, T.W., Stryakhilev, D., Lee, J.S., An, S.G., Pyo, Y.S., Lee, D.B., Mo, Y.G., Jin, D.U., and Chung, H.K. (2009). Flexible full color organic light-emitting diode display on polyimide plastic substrate driven by amorphous indium gallium zinc oxide thin-film transistors. Appl. Phys. Lett. *95*, 013503.

Patterson, M.J., Galloway, S.D., and Nimmo, M.A. (2000). Variations in regional sweat composition in normal human males. Exp. Physiol. *85*, 869–875.

Porchetta, A., Idili, A., Vallee-Belisle, A., and Ricci, F. (2015). General strategy to introduce pH-induced allostery in DNA-based receptors to achieve controlled release of ligands. Nano Lett. *15*, 4467–4471.

Rim, Y.S., Bae, S.H., Chen, H., Yang, J.L., Kim, J., Andrews, A.M., Weiss, P.S., Yang, Y., and Tseng, H.R. (2015). Printable ultrathin metal oxide semiconductor-based conformal biosensors. ACS Nano *9*, 12174–12181.

Rogers, J., Bao, Z., and Lee, T.W. (2019). Wearable bioelectronics: opportunities for chemistry. Acc. Chem. Res. *52*, 521–522.

So, H.M., Park, D.W., Jeon, E.K., Kim, Y.H., Kim, B.S., Lee, C.K., Choi, S.Y., Kim, S.C., Chang, H., and Lee, J.O. (2008). Detection and titer estimation of *Escherichia coli* using aptamer-functionalized single-walled carbon-nanotube field-effect transistors. Small *4*, 197–201.

Sonner, Z., Wilder, E., Heikenfeld, J., Kasting, G., Beyette, F., Swaile, D., Sherman, F., Joyce, J., Hagen, J., Kelley-Loughnane, N., et al. (2015). The microfluidics of the eccrine sweat gland, including biomarker partitioning, transport, and biosensing implications. Biomicrofluidics *9*, 031301.

Sorgenfrei, S., Chiu, C.Y., Gonzalez, R.L., Jr., Yu, Y.J., Kim, P., Nuckolls, C., and Shepard, K.L. (2011). Label-free single-molecule detection of DNA-hybridization kinetics with a carbon nanotube field-effect transistor. Nat. Nanotechnol. *6*, 126–132.

Sprigle, S., Linden, M., McKenna, D., Davis, K., and Riordan, B. (2001). Clinical skin temperature measurement to predict incipient pressure ulcers. Adv. Skin Wound Care *14*, 133–137.

Torrente-Rodriguez, R.M., Tu, J., Yang, Y., Min, J., Wang, M., Song, Y., Yu, Y., Xu, C., Ye, C., IsHak, W.W., et al. (2020). Investigation of cortisol dynamics in human sweat using a graphene-based wireless mHealth system. Matter *2*, 921–937.

Wang, H., Wang, B., Normoyle, K.P., Jackson, K., Spitler, K., Sharrock, M.F., Miller, C.M., Best, C., Llano, D., and Du, R. (2014). Brain temperature and its fundamental properties: a review for clinical neuroscientists. Front. Neurosci. *8*, 307.

Wang, S., Xu, J., Wang, W., Wang, G.N., Rastak, R., Molina-Lopez, F., Chung, J.W., Niu, S., Feig, V.R., Lopez, J., et al. (2018). Skin electronics from scalable fabrication of an intrinsically stretchable transistor array. Nature *555*, 83–88.

Webb, R.C., Bonifas, A.P., Behnaz, A., Zhang, Y., Yu, K.J., Cheng, H., Shi, M., Bian, Z., Liu, Z., Kim, Y.S., et al. (2013). Ultrathin conformal devices for precise and continuous thermal characterization of human skin. Nat. Mater. *12*, 938–944.

Weiss, P.S. (2013). President obama announces the brain initiative. ACS Nano *7*, 2873–2874.

Wen, X., Wang, B., Huang, S., Liu, T.L., Lee, M.S., Chung, P.S., Chow, Y.T., Huang, I.W., Monbouquette, H.G., Maidment, N.T., et al. (2019). Flexible, multifunctional neural probe with liquid metal enabled, ultra-large tunable stiffness for deep-brain chemical sensing and agent delivery. Biosens. Bioelectron. *131*, 37–45.

Willner, I., and Zayats, M. (2007). Electronic aptamer-based sensors. Angew. Chem. Int. Ed. *46*, 6408–6418.

Yang, H., Thompson, A.B., McIntosh, B.J., Altieri, S.C., and Andrews, A.M. (2013). Physiologically relevant changes in serotonin resolved by fast microdialysis. ACS Chem. Neurosci. *4*, 790–798.

Yang, H., Sampson, M.M., Senturk, D., and Andrews, A.M. (2015). Sex- and SERT-mediated differences in stimulated serotonin revealed by fast microdialysis. ACS Chem. Neurosci. *6*, 1487–1501.

Yang, Y., Song, Y., Bo, X., Min, J., Pak, O.S., Zhu, L., Wang, M., Tu, J., Kogan, A., Zhang, H., et al. (2020). A laser-engraved wearable sensor for sensitive detection of uric acid and tyrosine in sweat. Nat. Biotechnol. *38*, 217–224.

Yu, K.J., Kuzum, D., Hwang, S.W., Kim, B.H., Juul, H., Kim, N.H., Won, S.M., Chiang, K., Trumpis, M., Richardson, A.G., et al. (2016). Bioresorbable silicon electronics for transient spatiotemporal mapping of electrical activity from the cerebral cortex. Nat. Mater. *15*, 782–791.

Zhao, C., Xu, X., Bae, S.H., Yang, Q., Liu, W., Belling, J.N., Cheung, K.M., Rim, Y.S., Yang, Y., Andrews, A.M., et al. (2018). Large-area, ultrathin metal-oxide semiconductor nanoribbon arrays fabricated by chemical lift-off lithography. Nano Lett. *18*, 5590–5595.

Zhao, Y., Wang, B., Hojaiji, H., Wang, Z., Lin, S., Yeung, C., Lin, H., Nguyen, P., Chiu, K., Salahi, K., et al. (2020). A wearable freestanding electrochemical sensing system. Sci. Adv. *6*, eaaz0007.

Zhou, T., Hong, G., Fu, T.M., Yang, X., Schuhmann, T.G., Viveros, R.D., and Lieber, C.M. (2017). Syringe-injectable mesh electronics integrate seamlessly with minimal chronic immune response in the brain. Proc. Natl. Acad. Sci. U S A *114*, 5894–5899.

iScience, Volume *23*

Supplemental Information

Flexible Multiplexed In_2O_3 Nanoribbon Aptamer-Field-Effect Transistors for Biosensing

Qingzhou Liu, Chuanzhen Zhao, Mingrui Chen, Yihang Liu, Zhiyuan Zhao, Fanqi Wu, Zhen Li, Paul S. Weiss, Anne M. Andrews, and Chongwu Zhou

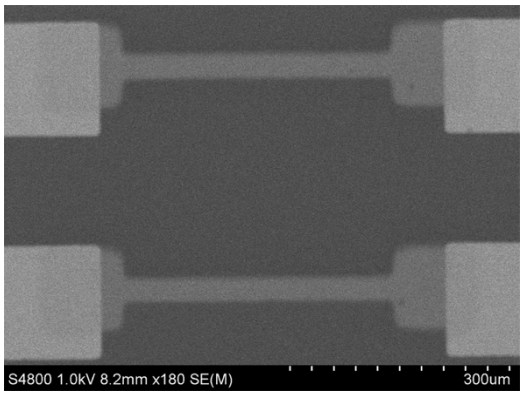

Figure S1. Scanning electron microscope image of two In_2O_3 nanoribbon field-effect transistors on a polyethylene terephthalate substrate. Each nanoribbon has a length of 500 μm and a width of 25 μm. Related to **Figure 1**.

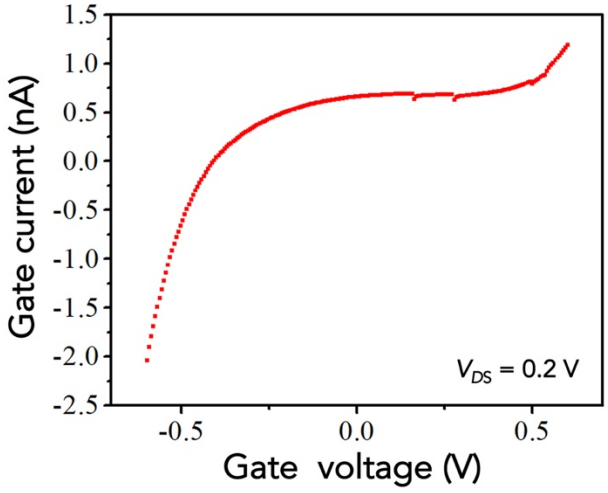

Figure S2. Gate leakage current *vs.* gate voltage from a representative In_2O_3 FET using a Au common gate. The gate leakage was negligible, and as shown, was smaller than 2 nA at V_{DS}=0.2 V. Related to **Figure 2**.

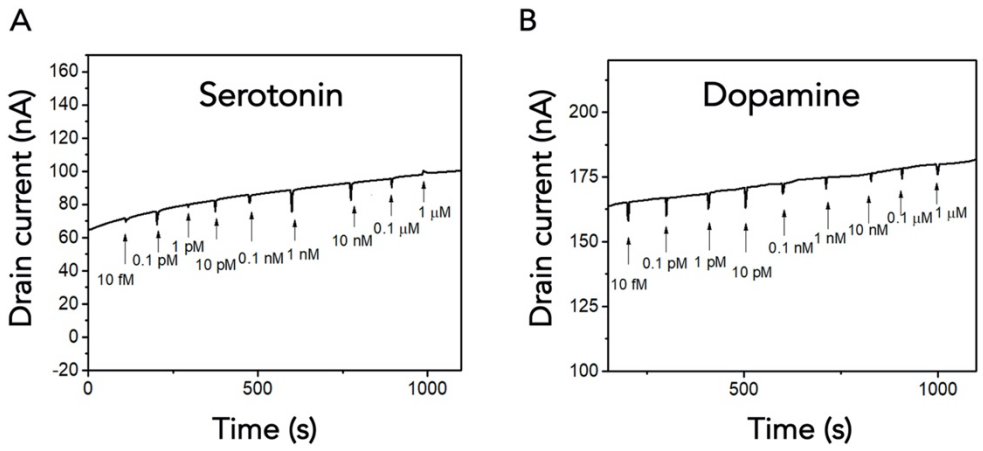

Figure S3. Control experiments for serotonin and dopamine sensing. The same sensing procedure was used at that in Figure 4 in the main text except sensors lacked (A) serotonin aptamers and (B) dopamine aptamers. Related to **Figure 4**.

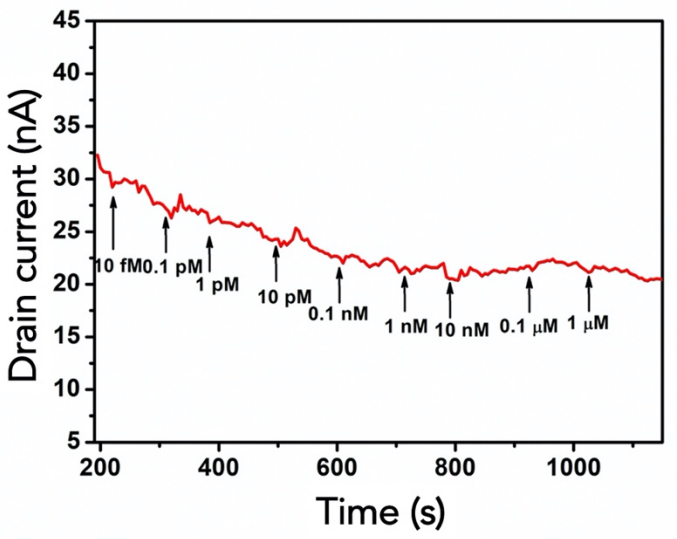

Figure S4. Control experiment with scrambled serotonin aptamer sequence for serotonin sensing.

Related to **Figure 4**.

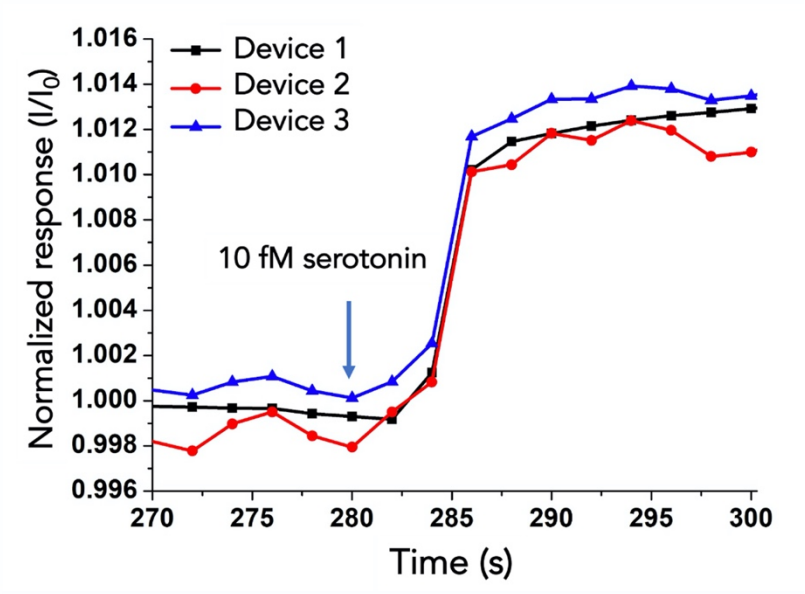

Figure S5. Temporal responses of In_2O_3 nanoribbon FETs to addition of 100 fM serotonin. Data are the same as those shown in Figure 4b in main text but are graphed to focus on temporal resolution for target sensing. Related to **Figure 4**.

Transparent Methods

Mobility calculation

The charge-carrier mobility of the In_2O_3 nanoribbon FETs is estimated using the following equation:

$$g_m = \frac{dI_D}{dV_{GS}} = \frac{W}{L} \cdot C_{DL} \cdot \mu_{FE} \cdot V_{DS}$$

where W is the channel width, L is the channel length, and C_{DL} is the electrical double layer capacitance per unit area in 0.1 M ionic strength aqueous solution (phosphate-buffered saline), reported previously as 25.5 μF cm^{-2} (Park et al., 2015). The maximum transconductance of 4.77 μS was obtained at a drain voltage of 0.2 V and a gate voltage of 0.43 V. The corresponding mobility is 18.7 cm^2 V^{-1} s^{-1}.

Tensile strain calculation

To calculate tensile strain when In_2O_3 nanoribbon FETs were wrapped tightly around a copper wire with a radius ~ 0.1 mm, we used the following formula:

$$\varepsilon = \frac{1}{R} \times \frac{d_s + d_f}{2} \times \frac{\chi \cdot \gamma^2 + 2 \cdot \chi \cdot \gamma + 1}{\chi \cdot \gamma^2 + \chi \cdot \gamma + \gamma + 1}$$

Here, R is the bending radius, d_s is the thickness of the substrate, d_f is the thickness of the In_2O_3 nanoribbon, $\gamma = d_f / d_s$ and $\chi = Y_f / Y_s$, where Y_f and Y_s are the Young's moduli of the In_2O_3 FET and substrate, respectively. If we assume $Y_f = Y_s$, the above equation can be simplified to:

$$\varepsilon = \frac{1}{R} \times \frac{d_s + d_f}{2}$$

The thickness of the polyethylene terephthalate (PET) substrate is 1.4 μm and the total thickness of the FET is less than 100 nm. With a bending radius of 0.1 mm, the tensile strain is calculated to be ~ 0.75 %.

Materials

All chemicals were purchased from Sigma-Aldrich Co. (St. Louis, MO), unless otherwise noted below. The SYLGARD 184 for fabricating polydimethylsiloxane (PDMS) wells and brain mimics was from Dow Corning Corporation (Midland, MI). Brain mimics were produced using silicone brain molds (Amazon #B003AQB2XK). The PDMS wells were made by cutting holes (~5 mm) in 3-mm PDMS sheets. The 1.4-μm-thick polyethylene terephthalate (PET) substrates were purchased from DuPont Teijin Films (Chester, VA) and used as received. Film thicknesses were measured and determined by the vendor using dielectric strength.

Physiological phosphate-buffered saline contained 137 mM NaCl, 2.7 mM KCl, 10 mM Na_2HPO_4, 1.8 mM KH_2PO_4. Artificial cerebrospinal fluid contained 147 mM NaCl, 3.5 mM KCl, 1 mM NaH_2PO_4, 2.5 mM $NaHCO_3$, 1 mM $CaCl_2$, and 1.2 mM $MgCl_2$. Oligonucleotides were obtained from Integrated DNA Technologies (Coralville, IA). Serotonin aptamer: 5'-/5ThioMC6-D/CGACTGGTAGGCAGATAGGGGAA GCTGATTCGATGCGTGGGTCG-3'. Serotonin scrambled aptamer: 5'-/5ThioMC6-D/CCCGG GAATTCCGGAATTGGGGCAATTGATGAGGGGGTCATGGG-3'. Dopamine aptamer: 5'-/5ThioMC6-D/CGACGCCAGTTTGAAGGTTCGTTCGCAGGTGTGGAGTGACGTCG-3'.

Device fabrication

Each 1.4-μm-thick PET film was attached to a rigid carrier wafer *via* a PDMS adhesion layer. The lamination was performed by attaching a corner of each PET film to a sacrificial PDMS layer, then aligning the edges. A soft scraper was used to smooth the attached film and to remove any bubbles. After immersing in consecutive acetone and isopropanol rinses for 15 min each, the first shadow mask was attached to each substrate to define the In_2O_3 nanoribbons. The In_2O_3 was deposited by RF sputtering (Denton Discovery 550 sputtering system). The nanoribbon thickness was controlled by the sputtering time. An In_2O_3 thickness of 16 nm was selected for all devices because this was the thinnest In_2O_3 layer that could be sputtered to give consistent device performance and high sensitivities to ion concentrations, *e.g.*, pH (Aroonyadet et al., 2015). Nanoribbon FETs with the same width and different thicknesses have been compared, where thinner nanoribbon FETs with higher surface-to-volume ratios showed the highest sensitivity to pH (Aroonyadet, et al., 2015).

The source, drain, and common gate electrodes, and temperature sensors were patterned using a second shadow mask. The bottom 1-nm Ti and top 50-nm Au layers were deposited *via* electron-beam (e-beam) evaporation. Device arrays were then peeled from their carrier wafers. Metal films deposited by e-beam evaporation were patterned using shadow masks, which is a cost-effective, cleanroom-free, and high-throughput process (Aroonyadet, et al., 2015; Liu et al., 2018). Moreover, this process does not result in In_2O_3 photoresist contamination or chemical exposure (Aroonyadet, et al., 2015). The thickness of the electrode metal layers impacts their performance. Previous studies indicated that the use of Au at 10-50 nm with a Ti adhesion layer of <5 nm provides robust flexibility with minimal cracking (Adrega et al., 2010; Seghir et al., 2015; Baetens et al., 2018). Graphene is another electrode candidate for flexible electronics. Graphene has been

deposited as a liquid-based mat and patterned by ink-jet printing or photolithography, the latter of which requires cleanroom processing and chemical exposure associated with the use of photoresist (Liu et al., 2014; Yang et al., 2016; Han et al., 2017; Song et al., 2017). Other conductive metal oxides that have been used for electrodes, such as indium-tin-oxide or fluorine-doped tin-oxide (Spechler et al., 2015; Yang, et al., 2016), have similar chemical properties as the channel material used here, *i.e.*, In_2O_3, which makes it challenging to functionalize channel regions separately from electrodes.

Surface functionalization

(3-Aminopropyl)trimethoxysilane and trimethoxy(propyl)silane 1:9 (v/v) were thermally evaporated using vapor-phase deposition onto In_2O_3 surfaces at 40 °C for 1 h followed by incubation in 1 mM ethanolic 1-dodecanethiol for 1 h to passivate Au electrodes. Substrates were rinsed in ethanol and immersed in 1 mM solutions of 3-maleimidobenzoic acid *N*-hydroxysuccinimide ester (MBS) dissolved in a 1:9 (v/v) mixture of dimethyl sulfoxide and PBS for 30 min. The MBS crosslinks amine-terminated silanes with thiolated DNA aptamers (Nakatsuka et al., 2018).

Aptamers (1 mM in nuclease-free water) were stored at -20 °C and diluted to 1 µM in nuclease-free water. Aptamers were heated for 5 min at 95 °C and cooled in an ice bath to room temperature. Substrates were rinsed with deionized water and immersed in 1 µM solutions of thiolated DNA aptamers overnight (~18 h), rinsed again with deionized water, and blown dry with N_2 gas before measurements. For multiplexed measurements, serotonin and dopamine aptamers (50 µL each) were added using a pipette onto two different adjacent devices. One FET on the

serotonin device was covered by a PDMS mask before adding the aptamer solution. The mask was then removed to expose an unfunctionalized FET, which served as a pH sensor.

Measurements

Each FET was connected with indium wires for electronic measurements. For the crumpling test, device arrays were crumpled tightly and held crumpled using tweezers for each crumpling cycle as shown in Fig. 3b. After ~5 s of crumpling, each array was then flattened. The crumpling and flattening cycles were repeated 100 times. Data were collected after 5, 10, 50, and 100 crumpling cycles. The concentrations of serotonin and dopamine tested were selected based on estimates of *in vivo* extracellular concentrations from our previous *in vivo* microdialysis measurements (Mathews et al., 2004; Yang et al., 2013; Yang et al., 2015). For multiplexed sensing, after using indium wires to connect the bonding pads of each FET, pH, serotonin, dopamine, and temperature sensors were covered with aCSF or different neurotransmitter solutions. Electrical characteristics under ambient conditions for the In_2O_3 FET devices were measured using an Agilent 4156B precision semiconductor parameter analyzer. Electrical characteristics in buffer and sensing results were measured with an Agilent B1500 semiconductor analyzer with capability to measure eight FETs at the same time (Ishikawa et al., 2009; Chang et al., 2011). Testing solutions of 300 μL were added to the PDMS wells. After each measurement, solutions were quickly removed using one pipette and the next testing solution was added immediately using a second pipette.

Supplemental references

Adrega, T.; Lacour, S. P. (2010). Stretchable gold conductors embedded in PDMS and patterned by photolithography: Fabrication and electromechanical characterization. *J. Micromech. Microeng. 20*, 055025.

Aroonyadet, N.; Wang, X.; Song, Y.; Chen, H.; Cote, R. J.; Thompson, M. E.; Datar, R. H.; Zhou, C. (2015). Highly scalable, uniform, and sensitive biosensors based on top-down indium oxide nanoribbons and electronic enzyme-linked immunosorbent assay. *Nano Lett. 15*, 1943–1951.

Baetens, T.; Pallecchi, E.; Thomy, V.; Arscott, S. (2018). Cracking effects in squashable and stretchable thin metal films on PDMS for flexible microsystems and electronics. *Sci. Rep. 8*, 9492.

Chang, H. K.; Ishikawa, F. N.; Zhang, R.; Datar, R.; Cote, R. J.; Thompson, M. E.; Zhou, C. (2011). Rapid, label-free, electrical whole blood bioassay based on nanobiosensor systems. *ACS Nano 5*, 9883–9891.

Han, T.-H.; Kim, H.; Kwon, S.-J.; Lee, T.-W. (2017). Graphene-based flexible electronic devices. *Mater. Sci. Eng. R Rep. 118*, 1–43.

Ishikawa, F. N.; Curreli, M.; Chang, H. K.; Chen, P. C.; Zhang, R.; Cote, R. J.; Thompson, M. E.; Zhou, C. (2009). A calibration method for nanowire biosensors to suppress device-to-device variation. *ACS Nano 3*, 3969–3976.

Liu, Q.; Liu, Y.; Wu, F.; Cao, X.; Li, Z.; Alharbi, M.; Abbas, A. N.; Amer, M. R.; Zhou, C. (2018). Highly sensitive and wearable In_2O_3 nanoribbon transistor biosensors with integrated on-chip gate for glucose monitoring in body fluids. *ACS Nano 12*, 1170–1178.

Liu, Y.; Zhou, H.; Cheng, R.; Yu, W.; Huang, Y.; Duan, X. (2014). Highly flexible electronics from scalable vertical thin film transistors. *Nano Lett. 14*, 1413–1418.

Mathews, T. A.; Fedele, D. E.; Coppelli, F. M.; Avila, A. M.; Murphy, D. L.; Andrews, A. M. (2004). Gene dose-dependent alterations in extraneuronal serotonin but not dopamine in mice with reduced serotonin transporter expression. *J. Neurosci. Methods 140*, 169–181.

Nakatsuka, N.; Yang, K. A.; Abendroth, J. M.; Cheung, K. M.; Xu, X.; Yang, H.; Zhao, C.; Zhu, B.; Rim, Y. S.; Yang, Y., et al. (2018). Aptamer-field-effect transistors overcome Debye length limitations for small-molecule sensing. *Science 362*, 319–324.

Park, S.; Lee, S.; Kim, C.-H.; Lee, I.; Lee, W.-J.; Kim, S.; Lee, B.-G.; Jang, J.-H.; Yoon, M. H. (2015). Sub-0.5 V highly stable aqueous salt gated metal oxide electronics. *Sci. Rep. 5*, 13088.

Seghir, R.; Arscott, S. (2015). Controlled mud-crack patterning and self-organized cracking of polydimethylsiloxane elastomer surfaces. *Sci. Rep. 5*, 14787.

Song, D.; Mahajan, A.; Secor, E. B.; Hersam, M. C.; Francis, L. F.; Frisbie, C. D. (2017). High-resolution transfer printing of graphene lines for fully printed, flexible electronics. *ACS Nano 11*, 7431–7439.

Spechler, J. A.; Koh, T.-W.; Herb, J. T.; Rand, B. P.; Arnold, C. B. (2015). A transparent, smooth, thermally robust, conductive polyimide for flexible electronics. *Adv. Funct. Mater. 25*, 7428–7434.

Yang, H.; Thompson, A. B.; McIntosh, B. J.; Altieri, S. C.; Andrews, A. M. (2013). Physiologically relevant changes in serotonin resolved by fast microdialysis. *ACS Chem. Neurosci. 4*, 790–798.

Yang, H.; Sampson, M. M.; Senturk, D.; Andrews, A. M. (2015). Sex- and SERT-mediated differences in stimulated serotonin revealed by fast microdialysis. *ACS Chem. Neurosci. 6*, 1487–1501.

Yang, W.; Wang, C. (2016). Graphene and the related conductive inks for flexible electronics. *J. Mater. Chem. C 4*, 7193–7207.